

# Allosteric communication mediated by protein contact clusters: A dynamical model

Ahmed A. A. I. Ali,<sup>1, a)</sup> Emanuel Dorbath,<sup>1, a)</sup> and Gerhard Stock<sup>1, b)</sup>  
*Biomolecular Dynamics, Institute of Physics, University of Freiburg, 79104 Freiburg,  
 Germany*

(Dated: 28 August 2024)

Allostery refers to the puzzling phenomenon of long-range communication between distant sites in proteins. Despite its importance in biomolecular regulation and signal transduction, the underlying dynamical process is not well understood. This study introduces a dynamical model of allosteric communication based on “contact clusters”—localized groups of highly correlated contacts that facilitate interactions between secondary structures. The model shows that allostery involves a multi-step process with cooperative contact changes within clusters and communication between distant clusters mediated by rigid secondary structures. Considering time-dependent experiments on a photoswitchable PDZ3 domain, extensive (in total  $\sim 500 \mu\text{s}$ ) molecular dynamics simulations are conducted that directly monitor the photoinduced allosteric transition. The structural reorganization is illustrated by the time evolution of the contact clusters and the ligand, which effects the nonlocal coupling between distant clusters. A timescale analysis reveals dynamics from nano- to microseconds, which are in excellent agreement with the experimentally measured timescales.

## I. INTRODUCTION

The investigation of allostery, which accounts for the intriguing phenomenon of long-range communication between distant protein sites, has attracted considerable attention in both experimental and computational domains.<sup>1–8</sup> Considering its critical role in cellular signaling and as a target in pharmaceutical research, however, our basic understanding of the dynamic process underlying allostery remains surprisingly limited. The direct observation of allosteric transitions remains difficult, particularly due to the subtle nature of structural changes<sup>9–11</sup> and sampling limitations of molecular dynamics (MD) simulations.<sup>12</sup> Moreover, the few existing MD studies showing allosteric transitions are found to be difficult to interpret, because they typically involve the nonlinear and nonlocal response of many protein residues.<sup>13–18</sup> Most commonly, allosteric communication is explained by network models,<sup>19,20</sup> where the protein residues are the ‘nodes’ of the network and the ‘edges’ describe some inter-residue coupling. While these formulations have contributed considerably to our understanding of allostery, they are by design statistical models, rather than a dynamical model of the real-time evolution of an allosteric transition. In this work, we aim to develop such a dynamical model.

To gain an understanding of the dynamical process underlying allostery, it is helpful to focus on a simple model system that allows us to perform time-dependent experiments as well as MD simulations, which both may directly observe the allosteric transition. In this respect, PDZ domains have been extensively studied, because they are well-established and structurally conserved protein interaction modules involved in the regulation of

multiple receptor-coupled signal transduction processes, but at the same time have also been considered as isolated model systems of allosteric communication.<sup>21–27</sup> They share a common fold (Fig. 1a), which consists of two  $\alpha$ -helices and six  $\beta$ -strands, with the second  $\alpha$ -helix and the second  $\beta$ -strand forming the canonical ligand binding groove. Interestingly, the NMR study conducted by Petit et al.<sup>22</sup> demonstrated that the removal of an additional short  $\alpha$ -helix at the C-terminal of PDZ3 reduces ligand affinity by a factor of 21, thereby revealing allosteric communication between the C-terminal and ligand binding. In this sense, PDZ3 can be considered as one of the smallest allosteric proteins, because both the active site (the  $\alpha_3$ -helix) and the allosteric site (the binding pocket) are clearly defined.

Recently, Bozovic et al.<sup>28</sup> employed photoswitching of the  $\alpha_3$ -helix to trigger a conformational change in PDZ3, propagating from the  $\alpha_3$ -helix to the ligand-binding pocket. Using time-resolved vibrational spectroscopy, they obtained a timescale of 200 ns for the perturbation to traverse to the ligand, which was interpreted as the speed of signaling in this single-domain protein. To facilitate a microscopic understanding of these experiments, Ali et al.<sup>29</sup> conducted extensive MD simulations of the system. By identifying all inter-residue contacts that changed during these simulations, they found a network of contacts linking the  $\alpha_3$ -helix and the protein core, which mediated the observed conformational transition. Hence, the study provided a first idea of the atomistic mechanism and also roughly reproduced the experimentally observed timescales.

However, the transient infrared response of PDZ3 is much more complex than the single 200 ns component due to the ligand. In line with previous studies on photoswitchable proteins,<sup>11,15,30,31</sup> the experiments revealed intricate signals across multiple timescales, from picoseconds to milliseconds. These findings raise questions on the nature of the structural dynamics underlying the

<sup>a)</sup>A. Ali and E. Dorbath contributed equally to this work.

<sup>b)</sup>Electronic mail: stock@physik.uni-freiburg.de

timescales. What are these motions and are they associated with some function of the protein? Do they account for the allosteric communication from the initially excited  $\alpha_3$ -helix to distant sites, even farther than the ligand? Are these processes mediated by a network of inter-residue contacts as well?

In this work, we show that the experimentally observed multiple timescales can indeed be explained by long-distance communication between localized ensembles (or clusters) of inter-residue contacts. These clusters can be identified by a correlation analysis<sup>32</sup> that discriminates collective motions underlying functional dynamics from uncorrelated motion. While the contact clusters represent the flexible joints and hinges of the protein,<sup>33</sup> the long-range communication between these contact clusters is mediated by rigid secondary structures.<sup>34</sup> For example, we find a structural rearrangement of the  $\beta_1$ - $\beta_2$  loop, which is triggered by the photoswitching of the  $\alpha_3$ -helix at the other end of the protein (Fig. 1a). This gives rise to a dynamical model of allostery, where the initially induced structural strain on the protein causes a multi-step structural reorganization process, which consists of cooperative conformational transitions within a contact cluster and of the sequential communication between clusters.

## II. RESULTS AND DISCUSSION

All results shown are based on nonequilibrium MD data of the photoswitchable PDZ3 domain used in experiment,<sup>28</sup> combining  $90 \times 1 \mu\text{s}$ -long and  $22 \times 10 \mu\text{s}$ -long trajectories (in total  $\sim 1.5 \times 10^6$  MD frames), see Methods.

### A. Definition of contact clusters

The analysis of conformational dynamics requires the choice of input coordinates or features.<sup>35,36</sup> In particular inter-residue contact distances have been shown advantageous, as they may directly account for tertiary interactions and scale linearly with the size of the system.<sup>37</sup> Because typically only a small subset of those coordinates is involved in a specific biomolecular process, we want to discard the remaining uncorrelated motions or weakly correlated noise coordinates. To this end, we perform a MoSAIC correlation analysis,<sup>32</sup> which allows us to distinguish collective motions underlying functional dynamics and uncorrelated motions. Hence it provides a versatile feature selection method, which was successfully applied to identify relevant coordinates of the folding of HP35<sup>36</sup> and of the functional motion of T4 lysozyme.<sup>38</sup> While Ali et al.<sup>29</sup> merely used MoSAIC to identify the contact network between the photoexcited  $\alpha_3$ -helix and the protein core, in this work we extend the contact analysis to all regions of PDZ3.

In a first step, we identify all contacts between residues  $i$  and  $j$  from the MD data using a distance criterion, see Methods. We then calculate the linear correlation matrix

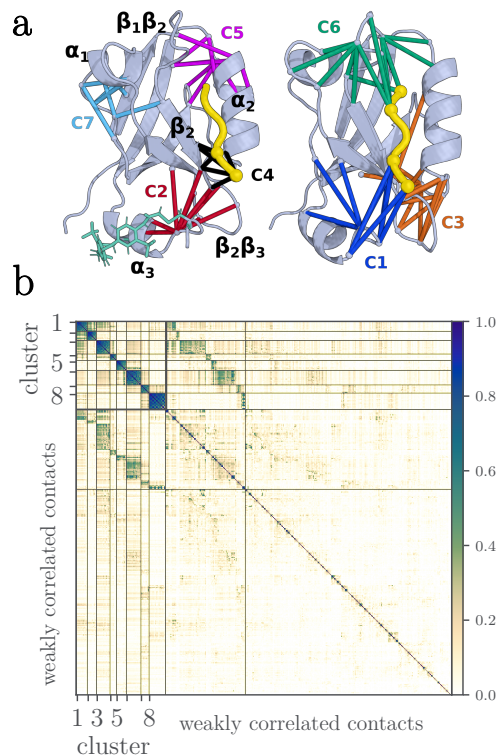


FIG. 1. (a) Photoswitchable PDZ3 domain,<sup>28</sup> indicating main secondary structural elements, the ligand (KETWV, yellow), and the azobenzene photoswitch (green, only shown on the left side). Inserted colored lines illustrate the contact distances associated with clusters C1 to C7 obtained from MoSAIC.<sup>32</sup> (b) Block-diagonal correlation matrix of PDZ3 obtained from MoSAIC clustering of all contact distances of PDZ3.

between contact distances  $r_{ij}$  and  $r_{kl}$ ,

$$\rho_{ij,kl} = \frac{\langle \delta r_{ij} \delta r_{kl} \rangle}{\langle \delta r_{ij}^2 \rangle^{1/2} \langle \delta r_{kl}^2 \rangle^{1/2}}, \quad (1)$$

where  $\delta r_{ij} = r_{ij} - \langle r_{ij} \rangle$  and the brackets  $\langle \dots \rangle$  denote a combined ensemble and time average over all MD data. To rearrange this matrix in an approximately block-diagonal form, we employ a community detection technique called Leiden clustering,<sup>39</sup> using the Python package MoSAIC<sup>32</sup> with a resolution parameter  $\gamma=0.5$ .

The resulting block-diagonal correlation matrix yields eight main blocks or clusters termed C1 to C8, see the upper left square of Fig. 1b. Within such a cluster, the coordinates are highly correlated (i.e., on average  $|\rho| \geq \gamma$ ), while the correlation between different clusters is low (i.e.,  $|\rho| < \gamma$ ). Moreover, we have contacts that are only weakly correlated (middle square) or hardly correlated (lower right square) with other contacts, and can therefore be omitted in the further analysis. This is, e.g., the case for stable contacts and contacts on the protein surface that form and break frequently. In the discus-

sion below, we also disregard cluster C8, whose contacts involve the N-terminus and are therefore highly fluctuating.

Figure 1a shows the contacts of clusters C1 to C7 inserted into the structure of PDZ3, where the numbering is chosen to roughly correspond to the spatial proximity of the clusters. Remarkably, we find that almost all cluster contacts mediate tertiary interactions between secondary structures. In this way, they represent the flexible joints and hinges of the protein,<sup>33</sup> which facilitate structural rearrangements. For example, the 11 contacts of C1 connect the  $\alpha_3$ -helix and the core of the protein, and thus control the alignment of the  $\alpha_3$ -helix to the protein. C2 also involves the  $\alpha_3$ -helix, as it connects Phe100 of  $\alpha_3$  to the  $\beta_2$ - $\beta_3$  loop. C3 helps to stabilize the  $\beta_2$ - $\beta_3$  loop through (up to) 14 interactions with  $\beta_4$ - $\alpha_2$ . The other main loop,  $\beta_1$ - $\beta_2$ , is stabilized via (up to) 16 contacts to the ligand and  $\beta_3$ - $\alpha_1$  in C6. Moreover, C4 connects the ligand to  $\beta_2$ , C5 bridges between  $\alpha_2$  and  $\beta_5$ , and C7 connects  $\beta_1$ - $\beta_2$  and  $\alpha_1$  to  $\alpha_1$ - $\beta_4$ . See Table S1 for a list of the contacts of all clusters, which also demonstrates the good stability of the clustering by comparing the outcome of different data sets. In particular, it is shown that we obtain qualitatively the same contact clusters from standard MD simulation of the *cis* and *trans* equilibrium states of the protein.

## B. Time evolution of contact clusters

Remarkably, the MoSAIC analysis achieves a partitioning of PDZ3 in weakly interacting clusters of correlated contacts. We now wish to study the nonequilibrium time evolution of these clusters, which follows the photoswitching of the  $\alpha_3$ -helix at time  $t = 0$  (see Methods). To this end, we introduce several observables that are averaged over all contacts of a cluster. We begin with the average change of the contact distances  $r_{ij}$  in a cluster, defined as

$$r_n(t) = \frac{1}{M_n} \sum_{i,j \in C_n} |\langle \Delta r_{ij}(t) \rangle_N|, \quad (2)$$

where  $\Delta r_{ij}(t) = r_{ij}(t) - r_{ij}(0)$ , the brackets  $\langle \dots \rangle_N$  denote the ensemble average over all  $N$  nonequilibrium trajectories, and  $M_n$  is the number of contact distances in cluster  $n$ . Note that we sum over the modulus of the distance changes, in order to avoid canceling effects. Displaying the time evolution of the cluster-averaged contact distances, Fig. 2a as expected shows a rapid and strong response of clusters C1 and the close-by C3. Interestingly, after about 100 ns, also the distant clusters C5 and C6 show a significant reaction. We stress that the time-delayed response of the distant contacts is a consequence of the initial photoswitching of cluster C1, and therefore represents a direct evidence for allosteric coupling. (For an equilibrium trajectory, we would find  $r_n(t) \approx \text{const.}$ )

We note that the finding of a significant response of the distant clusters C5 and C6 is somewhat unexpected,

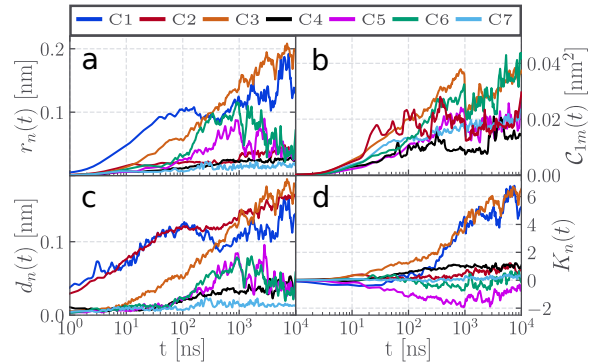


FIG. 2. Time evolution of (a) the contact distances  $r_n(t)$  averaged over cluster  $n$  [Eq. (2)], (b) the intercluster correlation  $C_{1m}(t)$  [Eq. (3)], (c) the corresponding cluster-averaged  $C_\alpha$ -distances  $d_n(t)$ , and (d) the average number of cluster contacts  $K_n(t)$ . We smoothed all log-time traces by a Gaussian filter function with a standard deviation of 6 frames. For  $t \leq 1\mu\text{s}$ , we average over 112 nonequilibrium MD trajectories, for  $t > 1\mu\text{s}$  over only 22 trajectories, which explains the large fluctuations at long times.

because the corresponding off-diagonal elements  $\rho_{ij,kl}$  of the correlation matrix [Eq. (1)] appear rather small in Fig. 1b. To explain this discrepancy, we define as alternative measure of the correlation between clusters  $n$  and  $m$  the quantity

$$C_{nm}(t) = \frac{1}{M_n M_m} \sum_{i,j \in C_n} \sum_{k,l \in C_m} |\langle \Delta r_{ij}(t) \Delta r_{kl}(t) \rangle_N|. \quad (3)$$

Displaying the time-dependent correlation  $C_{1m}(t)$  of cluster C1 with the other clusters, Fig. 2b clearly shows that apart from the close-by cluster C3 also the distant cluster C6 gets significantly excited due to the initial preparation of cluster C1. Note that the overall rise of the intercluster correlations  $C_{nm}(t)$  directly reflects the time evolution of the associated distances  $\Delta r_{ij}(t)$  and  $\Delta r_{kl}(t)$ . Apart from the missing time average and minor important normalization factors, the main difference to Eq. (1) is that we take in Eq. (3) the modulus of the correlation of each nonequilibrium trajectory. This prevents the canceling of positive and negative correlations of the individual trajectories.

Another quantity of interest is the average number of contacts  $K_n(t)$  of cluster  $n$ , see Fig. 2d. We find that only clusters C1 and the close-by C3 show a large change of  $K_n(t)$  (both form about 6 contacts), while the other clusters change only minor,  $|K_n(t) - K_n(0)| \lesssim 1$ . As an alternative distance measure, Fig. 2c finally shows the cluster-averaged  $C_\alpha$ -distances, which are mostly quite similar to the contact distances.

## C. Timescale analysis

The quantities shown in Fig. 2 exhibit dynamics on various timescales, ranging from nano- to microseconds.

To provide a well-defined measure for the timescales contained in such data, we model the underlying time series  $S(t)$  by a multiexponential response function<sup>30</sup>

$$S(t) = \sum_k s_k e^{-t/\tau_k}. \quad (4)$$

To this end, we choose the time constants  $\tau_k$  to be equally distributed on a logarithmic scale (e.g., 10 terms per decade) and fit the corresponding amplitudes  $s_k$  to the data, using a maximum-entropy regularization method,<sup>40</sup> see Methods.

To illustrate the distribution of timescales occurring in a cluster, we perform the timescale analysis for each contact distance  $r_{ij}(t)$  contained in the cluster, and define the timescale spectrum  $D_n(\tau_k)$  of cluster  $n$  as

$$D_n(\tau_k) = \sqrt{\sum_{i,j \in C_n} |s_k(i,j)|^2}, \quad (5)$$

which can be considered as the 'dynamical content' of the cluster.<sup>30</sup> As shown in Fig. 3a, clusters C1, C3 and C6 show overall the largest amplitudes, while the other clusters contribute significantly weaker. Referring to the local maxima as the 'main timescales' of the spectra, we find these timescales ranging from 30 ns to 3  $\mu$ s. Following photoswitching, clusters C1 and the close-by C2 and C3 naturally exhibit the earliest response at 30 ns. Less expected is that the second timescale at 200 ns is due to the distant clusters C6, C5 and C4 (in the order of their importance). At 800 ns we note the conformational transition of C1 aligning  $\alpha_3$  to the protein (see below), followed by transitions of the near-by clusters C2 and C3 at 1 and 1.1  $\mu$ s, respectively. Almost all clusters contribute to the slowest timescale of 3  $\mu$ s, with the largest contributions coming from clusters C6, C3, and C5.

Apart from studying the response of each contact cluster separately, we may also consider the response of the full system. To this end, we perform a timescale analysis of the contact distances of all seven clusters, and calculate the corresponding overall timescale spectrum  $D(\tau_k)$ . (Formally the cluster-specific spectra  $D_n(\tau_k)$  and the overall spectrum  $D(\tau_k)$  are related via  $D^2(\tau_k) = \sum_n |D_n(\tau_k)|^2$ .) As shown in Fig. 3b, the overall timescale spectrum exhibits well-defined peaks at 30 ns, 200 ns, and 3  $\mu$ s, as well as a broad shoulder at 800 ns, which all can be readily associated with the cluster-specific timescale spectra in Fig. 3a.

It is interesting to compare our calculated spectra to the experimental results by Bozovic et al.,<sup>28</sup> who inferred the timescale spectrum of PDZ3 from time-resolved infrared spectroscopy. Remarkably, they found well-defined peaks at 20 ns, 200 ns, 2  $\mu$ s and 20  $\mu$ s, as well as a broad feature in the decades following  $\sim$  1 ns and 200 ns. Our analysis reproduces perfectly the ligand-induced signal at 200 ns, and matches well the two intermediate times (30 vs. 20 ns) and (3 vs. 2  $\mu$ s). The 1 ns timescale of the experimental spectrum can most likely be explained by the initial 5 ns stretching of the

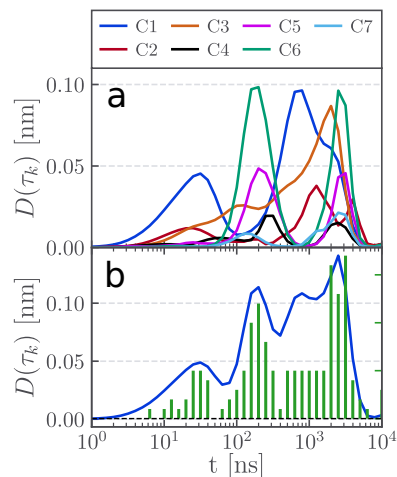


FIG. 3. (a) Timescale spectrum of contact distances  $r_{ij}(t)$ , obtained for clusters C1 to C7. (b) Overall timescale spectrum calculated for all clusters. Green bars indicate the number of contact distances, whose timescale analysis shows a maximum at the considered timescale.

$\alpha_3$ -helix (and the associated breaking of the contacts  $r_{28,102}$  and  $r_{97,102}$  at  $\lesssim$  1 ns, see below); these features are only weakly visible in Fig. 3. The diffuse region between the experimental peaks at 200 ns and 2  $\mu$ s seems to contain several contributions, which may be explained by the strongly overlapping timescale spectra of clusters C1 and C3. Lastly, the long experimental timescale of 20  $\mu$ s is clearly out of reach for our study.

#### D. Local response to photoswitching

We are now in a position to develop a mechanistic picture of the propagation of the initial perturbation of cluster C1 to the distant sites of the protein. The discussion is based on selected contact distances of the clusters shown in Fig. 4, while Fig. S1 provides comprehensive data of all these distances.

Prior to photoswitching, the system is prepared in the *cis* configuration, where the  $\alpha_3$ -helix is mostly stabilized by nonpolar contacts with the protein (e.g., Val28 and Tyr97 connect to Azo102). By attaching the azobenzene photoswitch to the side-chains of residues 95 and 102 of the  $\alpha_3$ -helix, Bozovic et al.<sup>28</sup> are able to switch the end-to-end distance of azobenzene from its twisted *cis* configuration (accommodating a stable helix) to the *trans* configuration (which destabilizes the helix). Following the sub-picosecond *cis-to-trans* photoisomerization of azobenzene at time  $t = 0$ , the photon energy is to a large part converted to vibrational energy of the helix. Since this kinetic energy is dissipated within tens of ps, it cannot disrupt the stabilizing contacts. The transport of vibrational energy via the backbone and the contacts of PDZ3, as well as the subsequent cooling of the protein in the solvent water, was measured by Baumann et al.<sup>41</sup>

and modeled in detail by Ishikura et al.<sup>42</sup> and Gulzar et al.<sup>43</sup>

What is more, the photoswitch also introduces a local conformational strain to the protein, which results in an increase of the potential energy, and subsequently relaxes through a sequence of processes on several timescales. In a first step, the photoswitching stretches the  $\alpha_3$ -helix on a 5 ns timescale,<sup>29</sup> which affects the stabilizing contacts  $r_{97,102}$  and  $r_{28,102}$  of cluster C1 (Fig. 4). Defining the breaking of a contact by  $\langle r_{ij}(t) \rangle \gtrsim 0.45$  nm,  $r_{28,102}$  breaks at  $t = 0.2$  ns, and  $r_{97,102}$  at 3 ns. The resulting destabilization of the  $\alpha_3$ -helix leads to the complete detachment of  $\alpha_3$  from the protein, which occurs on a timescale on 30 ns. This is evident from the rise of several distances of C1 up to a maximum at  $t \sim 100$  ns (Fig. 4). Hence we have shown that the peak at 30 ns of the C1 timescale spectrum (Fig. 3a) is caused by the photoinduced detachment of  $\alpha_3$ .

The other two timescales found for C1 are 800 ns which reflects the main conformational transition of C1, and a weaker feature at  $3 \mu\text{s}$ , which accounts for the structural relaxation of C1 towards the equilibrium state of the *trans* configuration. Most notably, the main conformational transition aligns  $\alpha_3$  to the protein, by cooperatively forming (at least) four new contacts, including three salt bridges [(Azo102,Lys55), (Lys103,Glu(-3)), (Lys103,Lys(-4))] and one hydrogen bond (Glu101,Lys(-4)).<sup>29</sup> (Residues are numbered from 1 to 103 for the protein and from -4 to 0 for the ligand.) This is evident from the decrease of all contact distances for  $t \gtrsim 100$  ns, see e.g.,  $r_{97,102}$  and  $r_{28,102}$  in Fig. 4. As shown by the mean number of contacts of C1 (Fig. 2), this process is only finished at  $t \sim 3 \mu\text{s}$ . While the previously used  $1 \mu\text{s}$ -long trajectories suggested a timescale of 300 ns for the conformational transition,<sup>29</sup> our  $10 \mu\text{s}$ -long data in fact yield a timescale of 800 ns. Considering the overall evolution from *cis* equilibrium ( $t < 0$ ), photoexcitation ( $t = 0$ ), conformational transition ( $t \sim 1 \mu\text{s}$ ), and relaxation towards *trans* equilibrium ( $t \gtrsim 3 \mu\text{s}$ ), cluster C1 describes an order-disorder-order transition.<sup>15</sup>

We turn to cluster C2, which is special as it only contains contacts involving residue 100 of the  $\alpha_3$ -helix (Fig. 1a). Contact partners are residues Glu96 and Tyr97 of  $\alpha_3$  and seven residues of the  $\beta_2$ - $\beta_3$ -loop (from Val28 to Gly35). The timescale spectrum of C2 shows two relatively weak signatures, a peak at 30 ns and a double-peak around  $2.5 \mu\text{s}$ , which originate from the contacts with  $\alpha_3$  and  $\beta_2\beta_3$ , respectively. Overall, though, C2 exhibits only minor changes of its contact distances, and therefore acts mostly as a quite rigid connection between the  $\alpha_3$ -helix of C1 and the  $\beta_2$ - $\beta_3$ -loop of C3.

Next to C1, cluster C3 is the other cluster that forms numerous new contacts (up to six) during its time evolution, see Fig. 2d. Consisting of 14 contact distances connecting the  $\beta_2$ - $\beta_3$ -loop (residues 29 - 36) and the  $\beta_4$ - $\alpha_2$ -loop (residues 67 - 71), this contact formation leads to a stabilization of the flexible  $\beta_2$ - $\beta_3$ -loop. Hence all distances are decreasing (e.g.,  $r_{33,69}$  in Fig. 4), with the

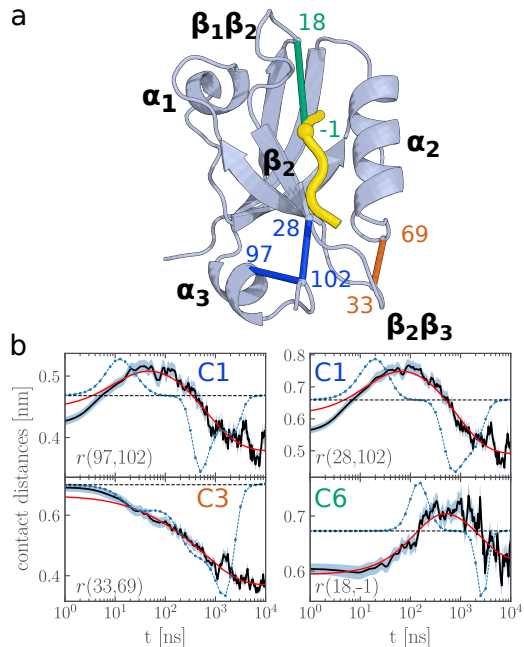


FIG. 4. (a) Structural description and (b) time evolution of selected contact distances of clusters C1, C3, and C6. MD data are drawn in black, the timescale spectrum [Eq. (5)] in blue, and the resulting fit of the data [Eq. (4)] in red. Residues are numbered from 1 to 103 for the protein and from -4 to 0 for the ligand.

exception of  $r_{29,71}$  reflecting the widening of the binding pocket due to the rearrangement of the ligand (Fig. S1). The timescale spectrum of C3 in Fig. 3a shows a broad distribution of times between 20 and 100 ns, as well as a well-defined peak at  $2 \mu\text{s}$ . This indicates that the initial excitation of the  $\alpha_3$ -helix travels from cluster C1 to cluster C3 either via rigid connections mediated, e.g., by cluster C2 and by the salt bridge Arg99-Glu34 (fast response), or as a consequence of the 800 ns conformational transition of C1 (slow response). In the latter case, about half of the conformational transitions of clusters C1 and C3 take place simultaneously (see Fig. S2), indicating possible cooperativity of these near-by contacts.

### E. Long distance propagation

The time evolution of the contact distances in Fig. 2a indicate also a clear response of several clusters that are distant to the initial photoexcitation of  $\alpha_3$ . This holds to some extent for clusters C4 and C5 along the  $\alpha_2$ -helix, and in particular for cluster C6, which we now focus on. With 15 contacts involving mostly the loops  $\beta_1$ - $\beta_2$  and  $\beta_3$ - $\alpha_1$ , cluster C6 is clearly at the other end of PDZ3. The time evolution of all contact distances of cluster C6 look very similar, see Fig. 4 for  $r_{18,-1}$  as a representative example (and Fig. S1 for all others). They show an initial increase on a 200 ns timescale, which peaks around

1  $\mu\text{s}$  and decays on a 2.5  $\mu\text{s}$  timescale. Accordingly, the timescale spectrum of C6 shows two well-defined peaks at 200 ns and 2.5  $\mu\text{s}$  (Fig. 3a). Since on average no new contacts are formed or broken (Fig. 2d), and since the final contact distances mostly return to their initial value, cluster C6 appears to respond elastically. While this is true for most contacts, however, a closer look shows that for  $\sim 70\%$  of the trajectories a new contact is formed between residues Arg18 and Gly83.

To facilitate this response, cluster C6 need to be in some way coupled to the initially perturbed cluster C1. For example, there are two contacts of C1 that couple to the  $\beta_2$  sheet (via residue Val28), which is connected to contacts of C6 involving the  $\beta_1$ - $\beta_2$ -loop (via residues Arg18 - Gly24). More importantly, though, both C1 and C6 are well connected to the ligand, comprising 5 ligand contacts of C1 and 6 ligand contacts of C6. To study how the ligand mediates the long-distant coupling between clusters C1 and C6, we consider the contacts of the protein with the five residues of the ligand. (See Fig. S3 for the time evolution of these contacts.) As shown in Fig. 5a, Lys(-4) and Glu(-3) are close to cluster C1, Thr(-2) is in the middle, and Trp(-1) and Val(0) are close to cluster C6. Accordingly, cluster C1 contains 2 ligand contacts with Lys(-4) and 3 with Glu(-3), while cluster C6 contains 4 ligand contacts with Trp(-1) and 2 with Val(0).

Performing a timescale analysis of the contact distances associated with the individual ligand residues, Fig. 5b shows that the main timescales of the contacts with Lys(-4) are very similar to the ones of cluster C1 (i.e., 30 and 800 ns), while the timescales of the contacts with Val(0) are very similar to the ones of cluster C6 (i.e., 200 ns and 2  $\mu\text{s}$ ). For the three inner ligand residues, we find both timescales to gradually shift between these two limiting cases. That is, the fast timescale (30 ns for Lys(-4)) shifts to a broad band covering  $\sim 10$  to 100 ns for Glu(-3), peaks around 100 ns for Thr(-2), and arrives at 200 ns for Trp(-1) and Val(0). The slow timescale (800 ns for Lys(-4)) evolves to a double peak at  $\sim 600$  ns and 2  $\mu\text{s}$  for Glu(-3), before it settles around 2  $\mu\text{s}$  for Trp(-1) and Val(0).

Hence the time-delayed response along the ligand indicates the propagation of the perturbation of cluster C1 to the distant cluster C6. In a first step, the detachment of  $\alpha_3$  at 30 ns appears to cause a response of C6 at 200 ns. The associated propagation time of  $\sim 170$  ns corresponds to the time it takes to transfer the structural strain of C1 via the ligand to C6. This is because this transport represents a diffusive process that involves the rearrangement of the conformation of the residues of the ligand and the surrounding protein. In a second step, the alignment of  $\alpha_3$  at 800 ns pulls the ligand contacts of C1 again in the opposite direction. This change also propagates through the ligand to cluster C6, and facilitates the relaxation of the cluster distances to their equilibrium value.

The response of the distant clusters is mainly elastic, that is, hardly any new contacts are formed to stabilize

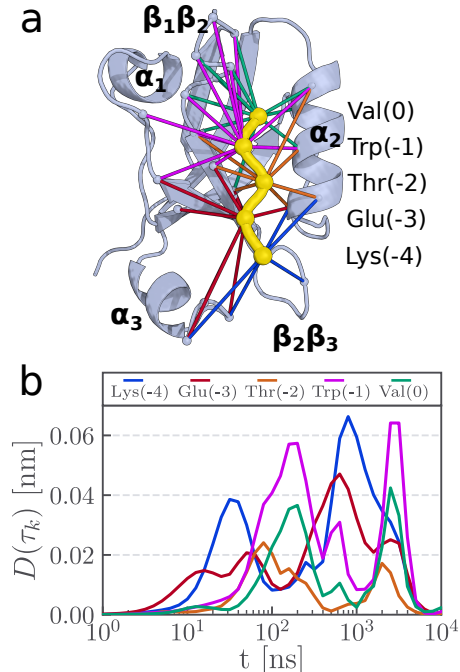


FIG. 5. (a) Inter-residue contacts of the ligand with PDZ3 and (b) their timescale spectrum.

the perturbed structure. However, if the  $\beta_1$ - $\beta_2$ - or  $\beta_3$ - $\alpha_1$ -loop of cluster C6 were involved in an interaction with another nearby molecule (e.g., a protein or co-factor, see Ref. 23), new contacts with this molecule could stabilize the allosteric response of cluster C6, resulting in an allosteric transition of C6 triggered by C1. For example, the Rho GTPase Cdc42 was shown to allosterically regulate Par-6 PDZ domain via binding to  $\beta_1$  and  $\alpha_1$ .<sup>44</sup>

Cluster C5 shares with C6 the same overall time evolution, i.e., an transient response at 200 ns, which decays on a timescale of 2.5  $\mu\text{s}$ , see Figs. 3a. Since C5 does not contain ligand contacts, the signal transmission most likely proceeds via the  $\alpha_2$ -helix and the four existing contacts with C6. Finally, clusters C4 and C7 show only a rather weak response to photoswitching (Fig. 2), and are therefore not considered here.

### III. CONCLUSIONS

On the basis of extensive (in total  $\sim 500 \mu\text{s}$ ) MD simulations and the identification of seven MoSAIC clusters of highly correlated tertiary contacts, we have outlined a contact cluster model of allosteric communication in PDZ3. Following an external perturbation (such as photoswitching or the (un)binding of a ligand), the protein experiences a structural strain that affects the nearby contact clusters. The subsequent multi-step structural reorganization process consists of cooperative conformational transitions within a cluster (Fig. 4), and of the communication between clusters (Fig. 5). The latter rep-

resents a sequential process that is mediated by rigid secondary structures. Hence we have shown that the response of the protein is in general nonlinear (since contacts are broken and formed in the clusters), and nonlocal (since rigid secondary structures connect distant clusters).

This general picture of allostery is corroborated by the timescale spectra of the contact clusters (Fig. 3) and the ligand contacts (Fig. 5), which illustrate the time evolution of the multi-step process. We have found excellent overall agreement between simulation and experiment,<sup>28</sup> which supports the general idea that experimental and computational observables essentially correspond to different projections of the underlying transfer operator and therefore give similar timescales.<sup>45</sup>

It is instructive to contrast the contact cluster model with commonly used network models,<sup>19,20</sup> which describe allosteric communication in terms of an interaction matrix of the protein residues. As an example of a quite elaborate approach, we mention the work of Hamelberg and coworkers,<sup>46</sup> which is also based on inter-residue contacts. Performing MD simulations of the allosteric states (e.g., active and inactive) of various systems, their interaction matrix is constructed from the contact changes due to the allosteric transition. As in most network approaches, subsequently a path analysis is applied to the network, which yields the presumably most important 'allosteric pathways' from the source of the perturbation to the target site.

Although our formulation bears some resemblance with this model of contact changes, it is constructed from the structural evolution revealed by the MD simulations, rather than from an empirical path analysis. Network paths are given as a sequence of inter-residue transitions, and as such cannot account for several main aspects of the dynamical process underlying allostery. That is, the cooperativity of contact changes (occurring in clusters), the nonlocality of the (inter-cluster) interactions which couple remote residues, and the possibility that several structural changes occur simultaneously in a trajectory. While allosteric pathways of network models may be a powerful tool, e.g., to predict the effects of mutations, they do not necessarily reflect the time evolution of a MD trajectory.

The discussion above indicates that the overall picture of allostery mediated by communicating contact clusters may be applicable to other allosteric systems. In particular, we have found that the construction of contact clusters does not necessarily require long MD data covering the allosteric transition, but can be also achieved from standard equilibrium simulation of the two allosteric states of the protein (e.g., the *cis* and *trans* states of photoswitchable PDZ3, see Tab. S1). To identify rigid secondary structure elements that couple different clusters, a rigidity analysis<sup>34</sup> may be employed. The resulting model may provide a qualitative description of possible allosteric mechanisms for a given system. These insights may also be useful in order to identify low-dimensional

biasing coordinates, which can be used by enhanced sampling techniques<sup>12</sup> that facilitate the observation of allosteric transitions in large biomolecular systems.

## IV. METHODS

**MD simulations.** All simulations used the GRO-MACS v2020 software package,<sup>47</sup> the Amber99SB\*ILDN force field<sup>48</sup> and the TIP3P water model. As detailed in Ref. 29, we first ran  $8 \times 10 \mu\text{s}$ -long MD simulations of the *cis* and the *trans* equilibrium states of PDZ3. To study the time evolution of the system following *cis* to *trans* photoisomerization states of the azobenzene photoswitch, we sampled 100 statistically independent structures from the *cis* equilibrium simulations, performed at time  $t=0$  a potential-energy surface switching method<sup>49</sup> to mimic the ultrafast photoisomerization of azobenzene, and calculated  $100 \times 1 \mu\text{s}$ -long nonequilibrium trajectories, ten of which were extended to  $10 \mu\text{s}$ . Moreover, we chose new starting structures from the *cis* equilibrium runs after 4 and  $8 \mu\text{s}$ , and performed  $12 \times 10 \mu\text{s}$ -long nonequilibrium simulations. All trajectories were sampled with a time step of 0.2 ns, resulting in total in  $\sim 1.5 \cdot 10^6$  frames of the MD data.

**MoSAIC analysis.** First we identified the inter-residue contact of PDZ3 by assuming that a contact is formed if the distance  $r_{ij}$  between the closest non-hydrogen atoms of residues  $i$  and  $j$  is shorter than  $4.5 \text{ \AA}$ .<sup>36,37</sup> Moreover, we requested  $|i - j| > 2$  to neglect neighboring residues, and focused on contacts that are populated more than 10% of the simulation time. As detailed in Ref. 29, this resulted in 403 inter-residue contacts. To identify clusters of highly correlated contacts, we performed a MoSAIC analysis<sup>32</sup> as explained above. To assess the clearness of the definition of cluster, we repeated the MoSAIC analysis for short ( $1 \mu\text{s}$ ) nonequilibrium MD data<sup>29</sup> for long nonequilibrium MD data, for *cis* and *trans* equilibrium data, and for using the mutual information measure to calculate the correlation. As shown in Tab. S1 listing the contacts of all clusters for all choices, this led to only minor changes of the clusters.

**Timescale analysis.** Using a maximum-entropy regularization method,<sup>40</sup> we minimize  $\chi^2 - \lambda_{\text{reg}} S_{\text{ent}}$ , with the usual root mean square deviation  $\chi^2$  of the fit function to the data, the entropy-based regularization factor  $S_{\text{ent}}$ , and the regularization parameter chosen as  $\lambda_{\text{reg}} = 100$ . The convergence of the fit is improved by extending the time series by an additional time decade, with the extended value derived as average over half of the previous decade. To ensure an equal contribution of each decade, we transformed the linearly spaced data into logarithmic data with the same number of frames per decade.

## Author's contributions

All authors contributed equally to this work.

## Supplementary material

Includes a table of the contacts of all clusters, and figures showing the time evolution of all all considered contact distances.

## Acknowledgments

The authors thank Peter Hamm, Steffen Wolf, Georg Diez, Daniel Nagel and Sofia Sartore for helpful comments and discussions. This work has been supported by the Deutsche Forschungsgemeinschaft (DFG) within the framework of the Research Unit FOR 5099 “Reducing complexity of nonequilibrium” (project No. 431945604), the High Performance and Cloud Computing Group at the Zentrum für Datenverarbeitung of the University of Tübingen, the state of Baden-Württemberg through bwHPC and the DFG through grant no INST 37/935-1 FUGG (RV bw16I016), the Black Forest Grid Initiative, and the Freiburg Institute for Advanced Studies (FRIAS) of the Albert-Ludwigs-University Freiburg.

## Data Availability Statement

The clustering package MoSAIC is available at our group homepage <https://www.moldyn.uni-freiburg.de/software.html>. Trajectories and simulation structures are available from the authors upon reasonable request.

- <sup>1</sup>Gunasekaran, K., Ma, B. & Nussinov, R. Is allostery an intrinsic property of all dynamic proteins? *Proteins* **57**, 433–443 (2004). URL <http://dx.doi.org/10.1002/prot.20232>.
- <sup>2</sup>Bahar, I., Chennubhotla, C. & Tobi, D. Intrinsic dynamics of enzymes in the unbound state and relation to allosteric regulation. *Curr. Opin. Struct. Biol.* **17**, 633–640 (2007).
- <sup>3</sup>Cui, Q. & Karplus, M. Allostery and cooperativity revisited. *Prot. Sci.* **17**, 1295–1307 (2008).
- <sup>4</sup>Changeux, J.-P. Allostery and the Monod-Wyman-Changeux model after 50 years. *Ann. Rev. Biophys.* **41**, 103–133 (2012).
- <sup>5</sup>Motlagh, H. N., Wrabl, J. O., Li, J. & Hilser, V. J. The ensemble nature of allostery. *Nature (London)* **508**, 331–339 (2014).
- <sup>6</sup>Tsai, C. J. & Nussinov, R. A Unified View of “How Allostery Works”. *PLoS Comput. Biol.* **10** (2014).
- <sup>7</sup>Thirumalai, D., Hyeon, C., Zhuravlev, P. I. & Lorimer, G. H. Symmetry, rigidity, and allosteric signaling: From monomeric proteins to molecular machines. *Chem. Rev.* **119**, 6788–6821 (2019).
- <sup>8</sup>Wodak, S. J. *et al.* Allostery in its many disguises: From theory to applications. *Structure* **27**, 566–578 (2019).
- <sup>9</sup>Brüschweiler, S. *et al.* Direct observation of the dynamic process underlying allosteric signal transmission. *J. Am. Chem. Soc.* **131**, 3063–3068 (2009).
- <sup>10</sup>Mehrabani, P. *et al.* Time-resolved crystallography reveals allosteric communication aligned with molecular breathing. *Science* **365**, 1167–1170 (2019).
- <sup>11</sup>Bozovic, O., Jankovic, B. & Hamm, P. Using azobenzene photo-control to set proteins in motion. *Nat. Rev. Chem.* **6**, 112–124 (2022).
- <sup>12</sup>Mehdi, S., Smith, Z., Herron, L., Zou, Z. & Tiwary, P. Enhanced sampling with machine learning. *Annu. Rev. Phys. Chem.* **75**, 347–370 (2024).
- <sup>13</sup>Vesper, M. D. & de Groot, B. L. Collective dynamics underlying allosteric transitions in hemoglobin. *PLoS Comp. Biol.* **9**, e1003232 (2013).
- <sup>14</sup>Pontiggia, F. *et al.* Free energy landscape of activation in a signalling protein at atomic resolution. *Nat. Commun.* **6**, 7284 (2015).
- <sup>15</sup>Buchenberg, S., Sittel, F. & Stock, G. Time-resolved observation of protein allosteric communication. *Proc. Natl. Acad. Sci. USA* **114**, E6804–E6811 (2017).
- <sup>16</sup>Zheng, Y. & Cui, Q. Multiple pathways and time scales for conformational transitions in apo-adenylate kinase. *J. Chem. Theory Comput.* **14**, 1716–1726 (2018).
- <sup>17</sup>Ayaz, P. *et al.* Structural mechanism of a drug-binding process involving a large conformational change of the protein target. *Nat. Commun.* **14**, 1885 (2023).
- <sup>18</sup>Vossel, M., de Groot, B. L. & Godec, A. The allosteric lever: towards a principle of specific allosteric response (2023). 2311.12025.
- <sup>19</sup>Guo, J. & Zhou, H.-X. Protein allostery and conformational dynamics. *Chem. Rev.* **116**, 6503–6515 (2016).
- <sup>20</sup>Dokholyan, N. V. Controlling allosteric networks in proteins. *Chem. Rev.* **116**, 6463–6487 (2016).
- <sup>21</sup>Fuentes, E., Der, C. & Lee, A. Ligand-dependent dynamics and intramolecular signaling in a PDZ domain. *J. Mol. Biol.* **335**, 1105–1115 (2004).
- <sup>22</sup>Petit, C. M., Zhang, J., Sapienza, P. J., Fuentes, E. J. & Lee, A. L. Hidden dynamic allostery in a PDZ domain. *Proc. Natl. Acad. Sci. USA* **106**, 18249–18254 (2009).
- <sup>23</sup>Ye, F. & Zhang, M. Structures and target recognition modes of PDZ domains: recurring themes and emerging pictures. *Biochem. J.* **455**, 1–14 (2013).
- <sup>24</sup>Gautier, C., Laursen, L., Jemth, P. & Gianni, S. Seeking allosteric networks in PDZ domains. *Protein Eng. Des. Sel.* **31**, 367–373 (2019).
- <sup>25</sup>Gerek, Z. N. & Ozkan, S. B. Change in Allosteric Network Affects Binding Affinities of PDZ Domains: Analysis through Perturbation Response Scanning. *PLoS Comput. Biol.* **7** (2011).
- <sup>26</sup>Kumawat, A. & Chakrabarty, S. Hidden electrostatic basis of dynamic allostery in a PDZ domain. *Proc. Natl. Acad. Sci. USA* **114**, E5825–E5834 (2017).
- <sup>27</sup>Faure, A. J. *et al.* Mapping the energetic and allosteric landscapes of protein binding domains. *Nature* **604**, 175–183 (2022).
- <sup>28</sup>Bozovic, O. *et al.* The Speed of Allosteric Signaling Within a Single-Domain Protein. *J. Phys. Chem. Lett.* **12**, 4262–4267 (2021).
- <sup>29</sup>Ali, A. A. A. I., Gulzar, A., Wolf, S. & Stock, G. Nonequilibrium modeling of the elementary step in PDZ3 allosteric communication. *J. Phys. Chem. Lett.* **13**, 9862–9868 (2022).
- <sup>30</sup>Stock, G. & Hamm, P. A nonequilibrium approach to allosteric communication. *Phil. Trans. B* **373**, 20170187 (2018).
- <sup>31</sup>Bozovic, O. *et al.* Real-time observation of ligand-induced allosteric transitions in a PDZ domain. *Proc. Natl. Acad. Sci. USA* **117**, 26031–26039 (2020).
- <sup>32</sup>Diez, G., Nagel, D. & Stock, G. Correlation-based feature selection to identify functional dynamics in proteins. *J. Chem. Theory Comput.* **18**, 5079–5088 (2022).
- <sup>33</sup>Papaleo, E. *et al.* The role of protein loops and linkers in conformational dynamics and allostery. *Chem. Rev.* **116**, 6391–6423 (2016).
- <sup>34</sup>Hermans, S. M., Pflieger, C., Nutschel, C., Hanke, C. A. & Gohlke, H. Rigidity theory for biomolecules: concepts, software, and applications. *WIREs Comput Mol Sci* **7**, e1311 (2017).
- <sup>35</sup>Ravindra, P., Smith, Z. & Tiwary, P. Automatic mutual information noise omission (AMINO): generating order parameters for molecular systems. *Mol. Syst. Des. Eng.* **5**, 339–348 (2020).
- <sup>36</sup>Nagel, D., Sartore, S. & Stock, G. Selecting features for Markov modeling: A case study on HP35. *J. Chem. Theory Comput.* **19**, 3391–3405 (2023).
- <sup>37</sup>Ernst, M., Sittel, F. & Stock, G. Contact- and distance-based principal component analysis of protein dynamics. *J. Chem. Phys.* **143**, 244114 (2015).
- <sup>38</sup>Post, M., Lickert, B., Diez, G., Wolf, S. & Stock, G. Cooperative protein allosteric transition mediated by a fluctuating transmis-



- sion network. *J. Mol. Bio.* **434**, 167679 (2022).
- <sup>39</sup>Traag, V., Waltman, L. & van Eck, N. From Louvain to Leiden: guaranteeing well-connected communities. *Sci. Rep.* **9**, 5233 (2019). <https://doi.org/10.1038/s41598-019-41695-z>.
- <sup>40</sup>Lórenz-Fonfría, V. A. & Kandori, H. Transformation of time-resolved spectra to lifetime-resolved spectra by maximum entropy inversion of the Laplace transform. *Appl. Spectrosc.* **60**, 407–417 (2006).
- <sup>41</sup>Baumann, T. *et al.* Site-resolved observation of vibrational energy transfer using a genetically encoded ultrafast heater. *Angew. Chem. Int. Ed. Engl.* **58**, 2899–2903 (2019).
- <sup>42</sup>Ishikura, T., Iwata, Y., Hatano, T. & Yamato, T. Energy exchange network of inter-residue interactions within a thermally fluctuating protein molecule: A computational study. *J. Comput. Chem.* **36**, 1709–1718 (2015).
- <sup>43</sup>Gulzar, A., Valiño Borau, L., Buchenberg, S., Wolf, S. & Stock, G. Energy transport pathways in proteins: A nonequilibrium molecular dynamics simulation study. *J. Chem. Theory Comput.* **15**, 5750 – 5757 (2019).
- <sup>44</sup>Peterson, F. C., Penkert, R. R., Volkman, B. F. & Prehoda, K. E. Cdc42 regulates the Par-6 PDZ domain through an allosteric CRIB-PDZ transition. *Mol. Cell* **13**, 665–676 (2004).
- <sup>45</sup>Noé, F. *et al.* Dynamical fingerprints for probing individual relaxation processes in biomolecular dynamics with simulations and kinetic experiments. *Proc. Natl. Acad. Sci. USA* **108**, 4822–4827 (2011).
- <sup>46</sup>Yao, X.-Q. & Hamelberg, D. Residue–residue contact changes during functional processes define allosteric communication pathways. *J. Chem. Theory Comput.* **18**, 1173–1187 (2022).
- <sup>47</sup>Abraham, M. J. *et al.* Gromacs: High performance molecular simulations through multi-level parallelism from laptops to supercomputers. *SoftwareX* **1-2**, 19 – 25 (2015).
- <sup>48</sup>Best, R. B. & Hummer, G. Optimized molecular dynamics force fields applied to the helix-coil transition of polypeptides. *J. Phys. Chem. B* **113**, 9004–9015 (2009).
- <sup>49</sup>Nguyen, P. H., Gorbunov, R. D. & Stock, G. Photoinduced conformational dynamics of a photoswitchable peptide: A nonequilibrium molecular dynamics simulation study. *Biophys. J.* **91**, 1224–1234 (2006).

# Supporting Information:

## Time-resolved allosteric communication between protein contact clusters

Ahmed A. A. I. Ali,<sup>†,‡</sup> Emanuel Dorbath,<sup>†,‡</sup> and Gerhard Stock<sup>\*,†</sup>

<sup>†</sup>*Biomolecular Dynamics, Institute of Physics, University of Freiburg, 79104 Freiburg,  
Germany*

<sup>‡</sup>*A. Ali and E. Dorbath contributed equally to this work.*

E-mail: [stock@physik.uni-freiburg.de](mailto:stock@physik.uni-freiburg.de)

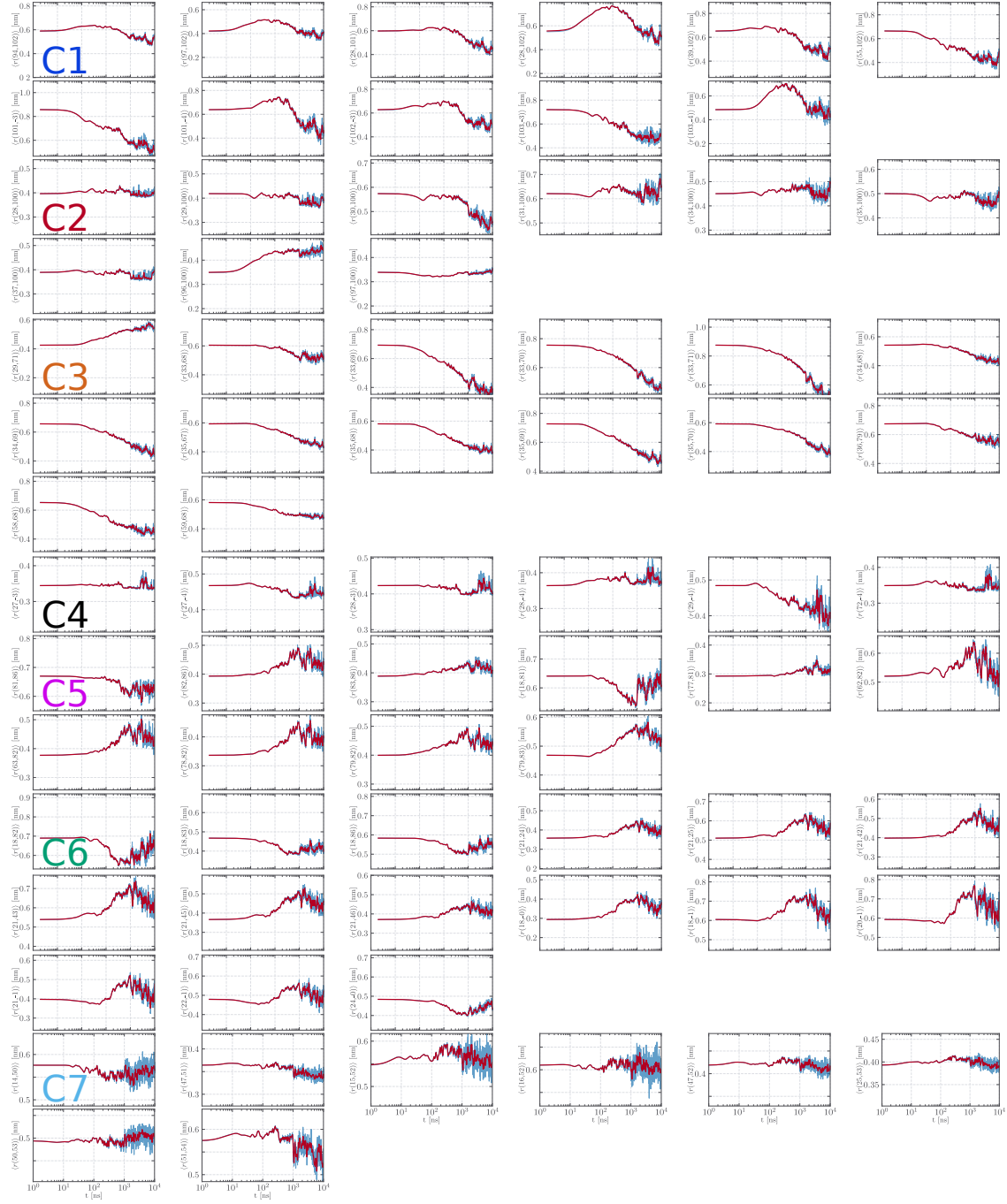


Figure S1: Averaged contact distances  $r_{ij}(t)$  for all 7 clusters, using a logarithmic Gaussian filter of  $\sigma = 6$  frames. The y-axis is chosen for each cluster such that it covers the same range around the initial position  $r_{ij}(t=0)$ . The blue line reflects the fluctuation from the unfiltered data while the red line correspond to the filtered data with  $\sigma=6$  frames.

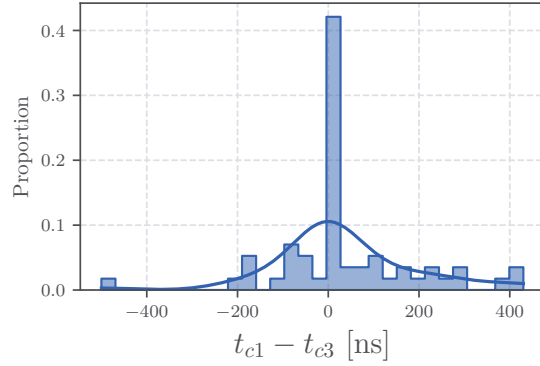


Figure S2: Histogram of the time difference ( $t_{C1}-t_{C3}$ ) between transition times in single  $1\ \mu\text{s}$  nonequilibrium trajectories in clusters C1 and C3 .The transition time is defined as the time required for a contact distance to change its status from high amplitude phase to contact phase (or vice versa) after the photoswitching event at  $t=0$ .

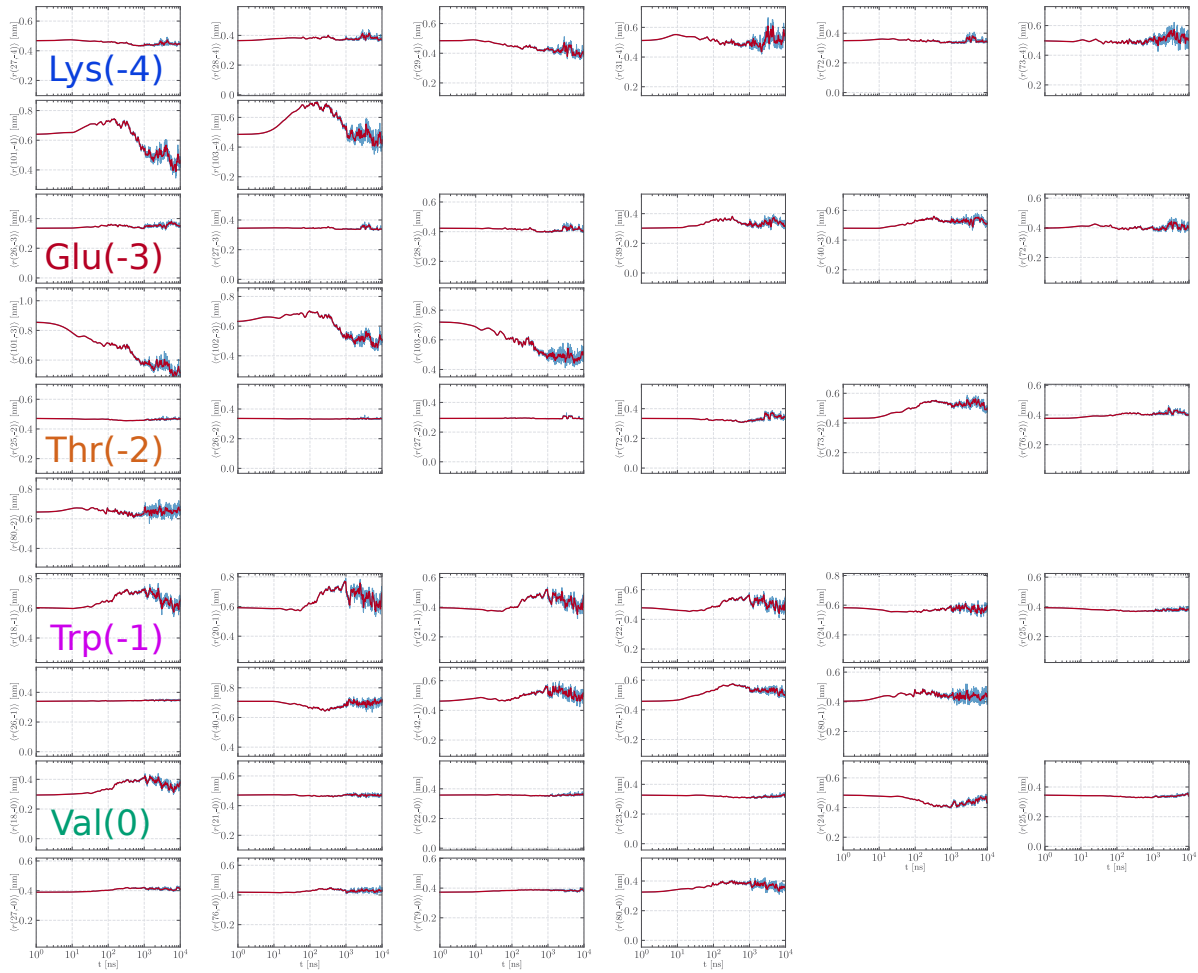


Figure S3: Averaged contact distances  $r_{ij}(t)$  for all contacts to the 5 ligand residues (total of 45 distances). A logarithmic Gaussian filter of  $\sigma = 6$  frames is used, and as above, the y-axis is set for all distances such that it covers the same range around the initial position.

## Comparison of MoSAIC clustering for different data sets

The following data sets are compared:

**‘Short NEQ’** contains  $100 \times 1 \mu s$  nonequilibrium trajectories. The contacts (in total 403) of this clustering (with Leiden resolution parameter  $\gamma = 0.5$ ) is shown in Fig. 1 in the main text. In Table.S1, the less important clusters C2, C4, C5 and C7 are only given for this data set, see below. For the most relevant clusters C1, C3 and C6, we also show the contact distances of three other data sets.

**‘Long NEQ’** contains  $22 \times 10 \mu s$  nonequilibrium trajectories with Leiden resolution parameter  $\gamma = 0.3$ .

**‘EQ’** contains  $0.5 \times 10^6$  MD frames for each *Cis* and *Trans* equilibrium simulations with  $\gamma = 0.4$ .

**‘Short NEQ/MI’** employ (instead of the linear correlation used above) the mutual information as correlation measure with  $\gamma = 0.03$ .

Table S1: List of contacts distances  $r_{ij}$  between residue  $i$  and  $j$  of Leiden clusters C1-C8. The result of four data sets are compared for C1, C3 and C6.

Cluster	Coordinates
1	
Short NEQ	$r_{94,102}, r_{97,102}, r_{28,101}, r_{28,102}, r_{39,102}, r_{55,102}, r_{101,(-3)}, r_{101,(-4)}, r_{102,(-3)},$ $r_{103,(-3)}, r_{103,(-4)}$
Long NEQ	$r_{94,98}, r_{94,102}, r_{95,99}, r_{97,102}, r_{28,101}, r_{28,102}, r_{39,97}, r_{39,102}, r_{55,102}, r_{101,(-3)},$ $r_{101,(-4)}, r_{102,(-3)}, r_{102,(-4)}, r_{103,(-3)}, r_{103,(-4)}$
EQ	$r_{94,102}, r_{97,102}, r_{28,101}, r_{28,102}, r_{39,102}, r_{101,(-3)}, r_{101,(-4)}, r_{102,(-3)}, r_{103,(-3)},$ $r_{103,(-4)}$
Short NEQ\MI	$r_{93,97}, r_{94,98}, r_{94,102}, r_{95,98}, r_{95,99}, r_{97,102}, r_{28,101}, r_{28,102}, r_{39,97}, r_{39,102}, r_{55,102},$ $r_{101,(-3)}, r_{101,(-4)}, r_{102,(-3)}, r_{103,(-3)}, r_{103,(-4)}$
3	
Short NEQ	$r_{29,71}, r_{33,68}, r_{33,69}, r_{33,70}, r_{33,71}, r_{34,68}, r_{34,69}, r_{35,67}, r_{35,68}, r_{35,69}, r_{35,70}, r_{36,79},$ $r_{58,68}, r_{59,68}$
Long NEQ	$r_{30,36}, r_{30,72}, r_{32,69}, r_{32,70}, r_{32,72}, r_{33,69}, r_{33,70}, r_{33,71}, r_{34,68}, r_{34,69}, r_{34,70}, r_{35,67},$ $r_{35,68}, r_{35,69}, r_{35,70}, r_{36,79}, r_{58,68}, r_{59,68}, r_{60,68}, r_{61,68}, r_{62,86}, r_{67,79}$
EQ	$r_{30,36}, r_{32,69}, r_{32,70}, r_{32,71}, r_{33,69}, r_{33,70}, r_{33,71}, r_{34,68}, r_{34,69}, r_{34,70}, r_{35,68}, r_{35,69},$ $r_{35,70}, r_{35,70}, r_{58,68}, r_{59,68}$
Short NEQ\MI	$r_{28,72}, r_{29,71}, r_{30,72}, r_{32,69}, r_{32,70}, r_{32,71}, r_{33,68}, r_{33,69}, r_{33,70}, r_{33,71}, r_{34,68}, r_{34,69},$ $r_{34,70}, r_{35,67}, r_{35,68}, r_{35,69}, r_{35,70}, r_{36,79}, r_{58,68}, r_{59,68}, r_{73,(-2)}$
6	
Short NEQ	$r_{18,82}, r_{18,83}, r_{18,86}, r_{21,24}, r_{21,25}, r_{21,42}, r_{21,43}, r_{21,45}, r_{21,46}, r_{18,(0)}, r_{18,(-1)},$ $r_{20,(-1)}, r_{21,(-1)}, r_{22,(-1)}, r_{24,(0)}$
Long NEQ	$r_{17,22}, r_{18,21}, r_{18,22}, r_{18,23}, r_{19,22}, r_{21,24}, r_{21,25}, r_{17,46}, r_{18,80}, r_{19,46}, r_{19,84}, r_{21,42},$ $r_{21,43}, r_{21,45}, r_{21,46}, r_{24,45}, r_{24,46}, r_{25,42}, r_{26,42}, r_{18,(0)}, r_{18,(-1)}, r_{20,(-1)}, r_{21,(-1)},$ $r_{22,(-1)}, r_{24,(0)}, r_{42,(-1)}$
EQ	$r_{18,21}, r_{19,22}, r_{21,24}, r_{21,25}, r_{19,84}, r_{21,42}, r_{21,43}, r_{21,45}, r_{21,46}, r_{18,(0)}, r_{18,(-1)},$ $r_{20,(-1)}, r_{21,(-1)}, r_{22,(-1)}, r_{24,(0)}, r_{42,(-1)}$
Short NEQ\MI	$r_{18,21}, r_{18,82}, r_{18,83}, r_{18,86}, r_{19,22}, r_{21,24}, r_{21,25}, r_{21,42}, r_{21,43}, r_{21,45}, r_{21,46}, r_{24,46},$ $r_{18,(0)}, r_{18,(-1)}, r_{20,(-1)}, r_{21,(-1)}, r_{22,(-1)}, r_{23,(0)}, r_{24,(0)}, r_{24,(-1)}, r_{25,(0)}, r_{42,(-1)}$

---

Cluster	Coordinates
2	$r_{28,100}, r_{29,100}, r_{30,100}, r_{31,100}, r_{34,100}, r_{35,100}, r_{37,100}, r_{96,100}, r_{97,100}$
4	$r_{27,(-3)}, r_{27,(-4)}, r_{28,(-3)}, r_{28,(-4)}, r_{29,(-4)}, r_{72,(-4)}$
5	$r_{81,86}, r_{82,86}, r_{83,86}, r_{18,81}, r_{77,81}, r_{62,82}, r_{63,82}, r_{78,82}, r_{79,82}, r_{79,83}$
7	$r_{47,51}, r_{47,52}, r_{14,50}, r_{50,53}, r_{51,54}, r_{16,52}, r_{15,52}, r_{25,53}$
8	$r_{1,95}, r_{2,95}, r_{1,98}, r_{2,51}, r_{1,51}, r_{1,102}, r_{2,98}, r_{2,52}, r_{3,54}, r_{2,102}, r_{1,100}, r_{1,48}, r_{3,95}, r_{2,94},$ $r_{2,53}, r_{2,54}, r_{2,97}$

---